主論文

学 位 申 請 論 文

Numerical and Theoretical Studies on Forced Two-Dimensional Turbulence on a Rotating Sphere

野 沢　徹

CONTENTS i

1 INTRODUCTION

For 2D turbulence on an infinite plane, Kraichnan[1] and Leith[2] theoretically predicted the energy spectrum that has two power laws of k^{-3} in the normal enstrophy-cascading range and of $k^{-5/3}$ in the upward energy-cascading range. Since then many numerical experiments have been done to examine several aspects of the 2D turbulence theory[3-5]. One of the most remarkable feature of the flow field obtained in the numerical experiments is the emergence of isolated coherent vortices in decaying 2D turbulence[6]. Characteristics of these coherent vortices have been investigated in detail using a surprisingly high-resolution model with 1024^2 grids[7].

A geophysical application of the 2D turbulence theory was firstly done by Rhines[8] with a numerical model on a β-plane to investigate the effect of the rotation of planets on the 2D turbulence. He showed that the upward energy cascade ceases roughly at a characteristic wavenumber $k_\beta = \sqrt{\beta/2U}$, where U is the r.m.s. velocity and β the meridional gradient of the Colioris parameter f. The conversion from turbulence into Rossby waves takes place around the wavenumber k_β. He also found that the flow field becomes anisotropic and a zonal band structure which consists of alternating easterly and westerly jets emerges owing to the β-effect. Another numerical experiment on decaying 2D turbulence on a β-plane was done by Holloway & Hendershott[9] to investigate the validity of their closure model. They showed that the flow field has a strong zonal anisotropy in the range of $k \lesssim k_\beta^H \equiv \beta/Z$, where Z is the r.m.s. vorticity. This tendency of the anisotropy in the range of $k \lesssim k_\beta$ was also obtained by Basdevant *et al.*[10] in the numerical experiments on the forced 2D turbulence on a β-plane. The flow field obtained by them is rather anisotropic in zonal direction in the high-wavenumber range of $k \gtrsim k_\beta$ as well as in the low-wavenumber range. Later, Shepherd[11] numerically studied the 2D turbulence on a β-plane under the existence of an imposed large-scale zonal jet. He showed that the disturbance energy is transferred into the range of $k \lesssim k_\beta$ owing to the shear-induced spectral transfer, and that the disturbance flow field becomes meridionally anisotropic in this low-wavenumber range.

Recently, Maltrud & Vallis[12] numerically studied the forced 2D turbulence on a β-plane with a high-resolution model (256^2 or 512^2 grids) under recent advanced computing facilities. In their experiments with low-wavenumber forcing, the anisotropy of the flow field increases as the strength of the β-effect increases, although the energy spectrum in the enstrophy-cascading range remains relatively unchanged (steeper than k^{-3}). An energy spectrum nearly proportional to $k^{-5/3}$ was also observed in the energy-cascading range in their experiments with high-wavenumber forcing. Vallis & Maltrud[13] showed that the obtained zonal band structure is extremely robust and persistent, and that the meridional scale of the obtained zonal jets becomes small as the strength of the β-effect increases. Similar zonal band structure that is robust and persistent was also found in the numerical experiments on a quasigeostrophic two-layer β-plane turbulence[14] forced by an imposed unstable vertical shear. In these experiments, the westerly jets are narrower and sharper than the easterly ones.

On the subject of the spectral anisotropy, Vallis & Maltrud[13] proposed a couple of transition curves from turbulent motion to wave-like behavior ; one of them is the "wave-turbulence boundary" obtained by equating the reciprocal of the eddy turnover time with the Rossby wave frequency. The curve of this boundary exhibits a characteristic dumbbell shape in the wavenumber space (k, l), and the 2D energy spectral density in their experiments with high-wavenumber forcing shows qualitatively similar dumbbell shape.

Nature of the 2D turbulence in spherical geometry is interesting because of the finiteness of the domain without any artificial lateral boundary, in addition to a possible application to planetary atmospheres. Williams[15] did a series of numerical experiments on the forced 2D turbulence on a rotating sphere, and he reproduced a zonal band structure similar to that of Jovian atmosphere for experimental conditions appropriate to Jupiter. However, the computational domain was restricted to $1/16$ of the entire sphere under the assumptions of longitudinal periodicity and equatorial symmetry, and the forcing function he adopted was not isotropic. Hence, the obtained band structure in the flow field might be influenced by the assumed boundary conditions and the anisotropic vorticity forcing. Another numerical experiment on the forced 2D turbulence on a rotating sphere was done by Basdevant *et al.*[10] to investigate the predictability properties of the flow field. In their experiments, however, the obtained flow field did not show such a strong zonality as that of Williams[15]. Recently, Yoden and Yamada[16] did a series of numerical experiments on the decaying 2D turbulence on a rotating sphere to investigate the effects of rotation and sphericity. They found an easterly jet in high latitudes for large rotation rates under the existence of Rossby waves, and the obtained flow field exhibits zonal anisotropy in all the latitudes. The initial flow in their experiment has a maximum of energy spectrum at a relatively low wavenumber $n = 10$ compared with that of the forcing ($n \sim 50$) used by Williams[15], so that the energy transfer in their decaying turbulence may be largely different from that in Williams' forced turbulence. In these studies on the spherical geometry, the spectral anisotropy was not investigated very much.

In this thesis, studies are intended to get deep understanding of the basic dynamics on the forced 2D turbulence on a rotating sphere. A series of numerical experiments is performed using a high-resolution full spherical model with a homogeneous and isotropic vorticity forcing. The sensitivity of the zonal band structure as well as that of the energy spectrum to two experimental paremeters of the rotation rate and the forcing wavenumber is studied. The forming process of the zonal band structure is investigated by dividing the flow field into zonal-mean and disturbance fields[17]. The anisotropic distribution of the 2D energy spectral density is examined on a spherical geometry[18]. The dependence of the spectral anisotropy on the β-effect is investigated by calculating the 2D energy density for the flow field which is orthographically projected on a tangential β-plane[18]. The numerical procedure is described in section 2, and results are given in section 3. Discussion is given in section 4, and conclusions are in section 5.

2 MODEL AND NUMERICAL PROCEDURE

Two-dimensional nondivergent flow on a rotating sphere is governed by a vorticity equation :

$$\frac{\partial \zeta}{\partial t} + \frac{1}{a^2} J(\psi, \zeta) + \frac{2\Omega}{a^2}\frac{\partial \psi}{\partial \lambda} = F + \nu\left(\nabla^2 + \frac{2}{a^2}\right)\zeta , \qquad (1)$$

where $\psi(\lambda, \mu, t)$ is a streamfunction field, $\zeta(\lambda, \mu, t) = \nabla^2\psi$: vorticity, λ: longitude, μ: sine latitude, t: time, ∇^2: horizontal Laplacian, $J(\psi, \zeta)$: horizontal Jacobian, a: radius of the sphere, Ω: rotation rate of the sphere, ν: kinematic viscosity coefficient, and $F(\lambda, \mu, t)$: vorticity forcing function. The second term of the viscosity term (i.e., $2/a^2$) is necessary to satisfy the conservation law of the total angular momentum. The radius and the rotation rate of the sphere are set to those of Jupiter; $a = 7.00 \times 10^7$m and $\Omega = \Omega_J = 1.76 \times 10^{-4}$rad s^{-1}. Time t is mea-

sured by Jovian day; 1 J.day = $2\pi/\Omega_J = 3.57 \times 10^4$s. The kinematic viscosity coefficient of $\nu = 5.00 \times 10^5 \mathrm{m^2 s^{-1}}$ is adopted as in Williams[15].

For the forcing function F, a random Markovian formulation is used as in Lilly[3] and Williams[15]:

$$F(\lambda, \mu, j\Delta t) = RF(\lambda, \mu, (j-1)\Delta t) + (1 - R^2)^{1/2} \widehat{F}(\lambda, \mu, j\Delta t) \,, \tag{2}$$

where R is a dimensionless memory coefficient ($R = 0.98$ as in Williams[15]), and $\widehat{F}$ is a randomly generated vorticity source at every time step. The random vorticity source function is defined as follows :

$$\widehat{F}(\lambda, \mu, j\Delta t) = \sum_{n=n_f-\Delta n}^{n_f+\Delta n} \sum_{\substack{m=-n \\ m\neq 0}}^{n} \widehat{F}_n^m(j) Y_n^m(\lambda, \mu) \,, \tag{3}$$

where $\widehat{F}_n^m(j)$ is an expansion coefficient of $\widehat{F}$ with spherical harmonics$Y_n^m(\lambda, \mu)$, which is determined so that it has random amplitude and phase at every time step j in order to construct a homogeneous and isotropic forcing. The forcing is given in a narrow range between $n_f - \Delta n$ and $n_f + \Delta n$ with $\Delta n = 2$, and the r.m.s. amplitude is held constant to $\mathrm{F} \equiv \sqrt{\langle \widehat{F}^2 \rangle}$ in each run, where $\langle \cdots \rangle$ denotes the spherical average. Figure 1 shows an example of the forcing field at a particular time step with $n_f = 40$.

A pseudospectral method with a triangular truncation of T199 ($n \leq 199 = N$) is used for the computation of the advection (Jacobian) term ; grids for the spectral transformation are 600 in longitudes and 300 in latitudes. Equation (1) is integrated from an initial condition of zero velocity field for a period of $t = 1000$ J.days. The Runge-Kutta-Gill method is used for the time integrations with $\Delta t = 0.05$ J.day. All of the computations are done in double precision.

Table I gives a summary of eighteen experiments which will be reported in this paper. We perform three series of the experiments; three values of the forcing wavenumber $n_f = 20$, 40, and 79 are chosen. For each forcing wavenumber, six values of the rotation rate are chosen: $\Omega/\Omega_J = 0.00$, 0.25, 0.50, 1.00, 2.00, and 4.00. The sphere has Ω/Ω_J rotations par unit J.day. The r.m.s. amplitude of the forcing F is determined by a method of trial and error to get a similar value of the total energy ($\mathcal{E} \approx 2.45 \times 10^3 \mathrm{m^2 s^{-2}}$) in the cases of no rotation, and the value is not changed for the runs with the same forcing wavenumber. The sequence of random numbers for the amplitude and phase of the vorticity source function is unchanged for all the experiments.

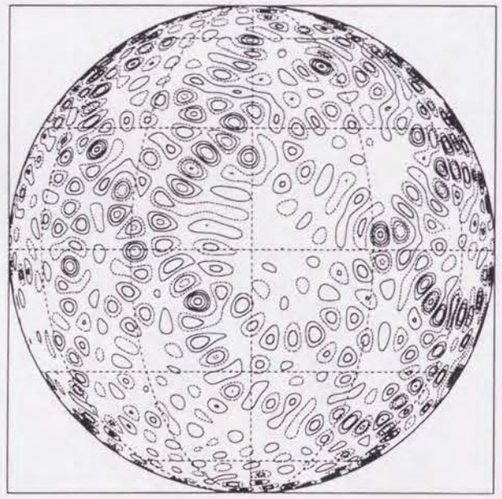

FIG. 1. Vorticity forcing field at $t = 100$ J.days with $n_f = 40$. Contour interval is 2.5×10^{-11} s^{-2} and negative areas are denoted by dotted lines. The zero contour has been deleted. Orthographic projection is used with the center at $\lambda = 0°$ and $\varphi = 0°$. Meridians and parallels are drawn for every 30°.

TABLE I. Summary of experiments. The column headings are given in the text.

series	run#	n_f	Ω/Ω_J	F ($\mathrm{s^{-2}}$)	$\mathcal{E}$ ($\mathrm{m^2 s^{-2}}$)	group	n_β	k_β	
								$\varphi_c = 0°$	$\varphi_c = \pm 45°$
I	1	20	0.00	7.85×10^{-12}	2.46×10^3	**A**	—	—	—
	2		0.25		2.34×10^3	**B**	5.95	1.205	0.937
	3		0.50		2.23×10^3	**B**	8.51	1.862	1.288
	4		1.00		1.76×10^3	**C**	12.77	3.136	1.917
	5		2.00		8.74×10^2	**C**	21.52	5.652	3.693
	6		4.00		3.97×10^2	**C**	37.06	10.024	6.549
II	7	40	0.00	2.18×10^{-11}	2.45×10^3	**A**	—	—	—
	8		0.25		2.52×10^3	**B**	5.84	1.255	0.933
	9		0.50		2.45×10^3	**B**	8.31	1.873	1.272
	10		1.00		2.15×10^3	**B**	12.14	2.449	1.871
	11		2.00		1.98×10^3	**B**	17.54	3.761	2.683
	12		4.00		1.03×10^3	**C**	29.18	7.695	4.352
III	13	79	0.00	7.85×10^{-11}	2.43×10^3	**A**	—	—	—
	14		0.25		2.56×10^3	**B**	5.82	1.187	0.918
	15		0.50		2.51×10^3	**B**	8.27	1.682	1.290
	16		1.00		2.55×10^3	**B**	11.65	2.658	1.922
	17		2.00		2.10×10^3	**B**	17.29	3.413	2.747
	18		4.00		1.64×10^3	**B**	25.99	5.079	4.098

3 RESULTS

3.1 Energy spectrum

Figure 2 shows the time-averaged energy spectrum $E(n)$:

$$E(n) = \frac{1}{2} \frac{n(n+1)}{a^2} \sum_{m=-n}^{n} \overline{|\, \psi_n^m(t) \,|^2} \,, \tag{4}$$

where $\psi_n^m(t)$ is an expansion coefficient of ψ with spherical harmonics $Y_n^m(\lambda, \mu)$:

$$\psi(\lambda, \mu, t) = \sum_{n=2}^{N} \sum_{m=-n}^{n} \psi_n^m(t) Y_n^m(\lambda, \mu) \,, \tag{5}$$

and an overbar indicates the time average from 800 to 1000 J.days. For all the experiments, the slope of the energy spectrum is close to n^{-4} in the enstrophy-cascading range of $n \gtrsim n_f$ independent of the rotation rate Ω and the forcing wavenumber n_f. When the forcing wavenumber is not large (series I and II), however, the slope in this range becomes a little steep as the rotation rate increases. An upward energy-cascading range is also obtained for all the experiments

except for a few runs of #4-6, and #12. The energy spectra are nearly proportional to $n^{-5/3}$ in this range, and the slope steepens slightly as Ω increases. In the case of no rotation (#1, #7, and #13), the energy spectrum is steeper than $n^{-5/3}$ at the low wavenumbers of $n \lesssim 7$ because the energy is accumulating in this range owing to the finiteness of the spherical domain. For the experiments with rotation, on the other hand, the spectrum does not obey the power law of $n^{-5/3}$ at low wavenumbers (the energy-cascading range becomes narrow), and the spectrum in this range becomes noisy as Ω increases. Here, a characteristic wavenumber n_β is introduced in the analogy of Rhines' k_β[8]:

$$n_\beta \equiv a \sqrt{\frac{\langle \beta \rangle}{2U}} , \tag{6}$$

where U is the r.m.s. velocity at t = 1000 J.days ($U = \sqrt{2\mathcal{E}}$), and $\langle \beta \rangle$ is the spherical average of β: $\langle \beta \rangle = \frac{1}{2}\int_{-1}^{1} \beta d\mu = \frac{\pi\Omega}{2a}$. At the horizontal scale of a/n_β, the nonlinear Jacobian term is comparable to the "β-term", $\frac{2\Omega}{a^2}\frac{\partial \psi}{\partial \lambda}$, in Eq.(1). Figure 2 shows that n_β indicated by an arrow

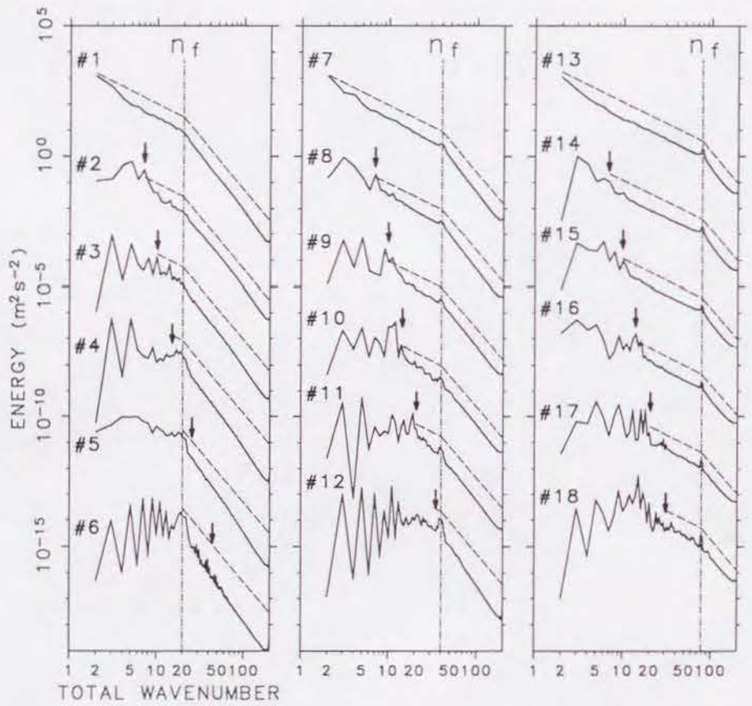

FIG. 2. Energy spectrum averaged from 800 to 1000 J.days. The number in the upper left of each curve represents the run number. The curves are arranged from left to right in the order of the forcing wavenumber n_f, and from top to bottom in the order of the rotation rate Ω/Ω_J ; each spectrum is successively shifted down by a factor of $10^{-3}\mathrm{m}^2\mathrm{s}^{-2}$ for clarity. Thin dot-dashed lines represent the forcing wavenumber n_f and thick arrows the wavenumber n_β at which scale the "β-term" is comparable to the nonlinear Jacobian term. A broken line of n^{-4} is added in the range of $n_f \le n \le N$ = 199 for all runs. Another broken line of $n^{-5/3}$ is also added in the range of $n_\beta \le n \le n_f$ except for the two runs of #5 and #6.

roughly gives the lower bound of the energy-cascading range. The spectrum does not show any clear power law in $2 \le n \lesssim n_\beta$, where the "β-term" is larger than the nonlinear term. When the forcing wavenumber is small and the rotation rate is large (#4-6, and #12), the wavenumber n_β is nearly equal to or larger than n_f, and the energy-cascading range with $n^{-5/3}$ power low is not found at all.

The energy flux functions for all runs are shown in Fig.3. The energy flux function $\Pi(n)$ is calculated from the energy transfer function $T(n)$:

$$\Pi(n) = \sum_{n'=2}^{n} T(n') , \tag{7}$$

$$T(n) = -\sum_{m=-n}^{n} \overline{\{\psi_n^m(t)\}^\dagger N_n^m(t)} , \tag{8}$$

where $N_n^m(t)$ is the expansion coefficient of the nonlinear Jacobian term, and $(\cdots)^\dagger$ denotes complex conjugate. In the case of no rotation (#1, #7, and #13), the energy flux is nearly constant in the range of $2 \le n \lesssim n_f$, so that the energy is transferred as far as the lowest wavenumber of n = 2. For the experiments with rotation except for #4-6, and #12, the energy flux function is parallel to that for no rotation in the energy-cascading range of $n_\beta \lesssim n \le n_f$ indicating that the effect of rotation is weak in this range, although $\Pi(n)$ is slightly steeper than that for no rotation

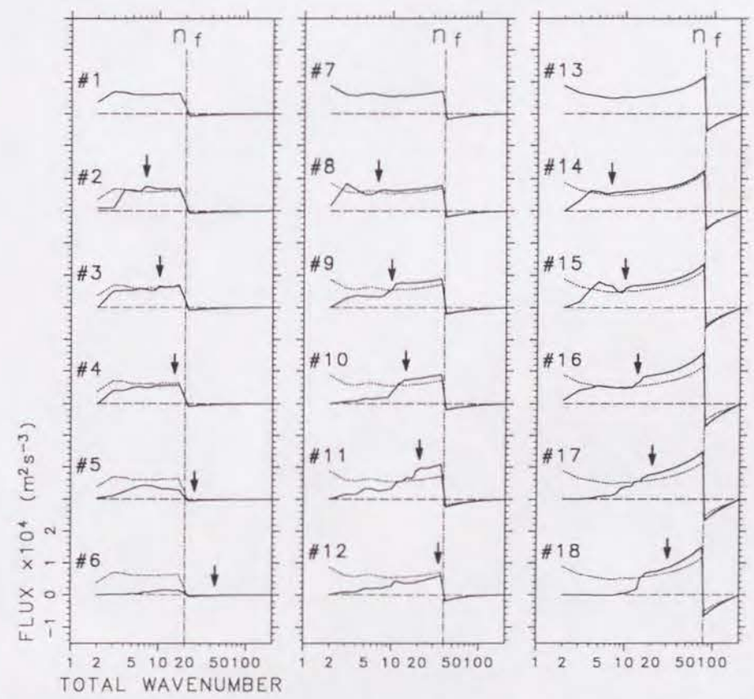

FIG. 3. Time-averaged energy flux function for the last 200 J.days. Broken lines are zero lines. The wavenumbers n_f (thin dot-dashed lines) and n_β (thick arrows) are the same as in Fig.2. Arrangement of the curves is identical to that of the curves in Fig.2. The energy flux function for the run without rotation (top curves in each panel) is superimposed on that for the other runs in the same series (thin dotted lines).

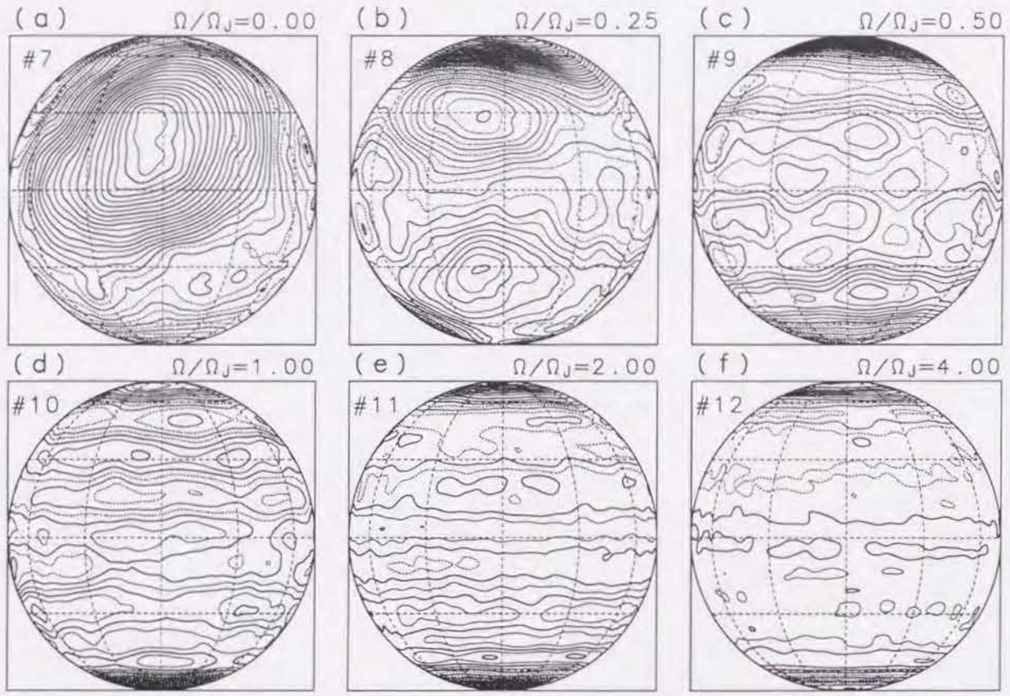

FIG. 4. Streamfunction field at t = 1000 J.days for the runs of series II. Contour interval is 2.5×10^8 m^{2}s^{-1} and negative areas are denoted by dotted lines. Map projection is the same as in Fig.1.

even in this range for the runs #17-18 with large Ω/Ω_J. In the range of $2 \leq n \lesssim n_\beta$, on the other hand, the energy flux function is not parallel to that of no rotation but it has a large decline ; the energy transfer is largely suppressed in this range beyond n_β. When the forcing wavenumber is small and the rotation rate is large (#4-6, and #12), the energy flux is smaller than that for no rotation in the range of $2 \leq n \lesssim n_f$; the upward energy cascade is strongly suppressed by the rotation even from the forcing region.

3.2 Flow field

The streamfunction field $\psi(\lambda, \mu, t)$ at t = 1000 J.days is shown in Fig.4 for six values of Ω/Ω_J in the series II experiments with $n_f = 40$. In the case of no rotation (a), the streamfunction field has a very large pattern that is characterized by the lowest wavenumber n = 2 owing to the upward energy cascade as shown in Figs.2 and 3. This flow pattern moves irregularly on the sphere without changing the pattern largely. For the experiments with rotation (b-f), on the other hand, zonal band structures become dominant in the streamfunction field. The zonality of the streamfunction field increases as the rotation rate increases. Although details of the flow patterns change with time, the zonal structures do not change particularly for large rotation rates. The amplitude of ψ is large in high latitudes, forming a circumpolar vortex. The edge of the polar vortex shifts to higher latitudes as the rotation rate increases. In the rest of the streamfunction field outside of the polar vortex, the amplitude of ψ decreases as Ω increases and the zonal band structure becomes unclear in middle and low latitudes for the most rapidly rotating case (f).

The relative vorticity field $\zeta(\lambda, \mu, t)$ at t = 1000 J.days is shown in Fig.5 for the same runs as in Fig.4 (series II). In the case of no rotation (a), several coherent vortices emerge in the flow field, one of which corresponds to a cluster of negatively large patches near $(\lambda, \varphi) = (-10°, 30°)$. Typical size of the cluster is larger than that of the forcing (see Fig.1) suggesting merging processes of the vorticity patches. A lot of patches of large vorticity with both signs have a rather circular structure with similar size as that of the forcing. A lot of filament structures are also seen in the rest of the vorticity field, indicating that the fluid motions are largely turbulent there. For the experiments with rotation (b-f), on the other hand, the pattern of the vorticity field is very different from that without rotation. When the rotation rate is small (b), the coherent vortices in the flow field get elongated zonally in middle and low latitudes, although a coherent vortex can be seen in high latitudes because of the weakness of the "β-effect" in the polar region. Patches of large vorticity are also elongated zonally in middle latitudes. In the cases with moderate rotation rate (c-e), the elongation takes place in all the latitudes, and the alternating positive and negative vorticity bands emerge. As the rotation rate increases, the number of the vorticity bands increases and the width of them decreases in accordance with the formation of zonal band structures. For large Ω (f), the vorticity band structure and the elongated vortices are confined in high latitudes whereas nearly circular vortices emerge in middle and low latitudes.

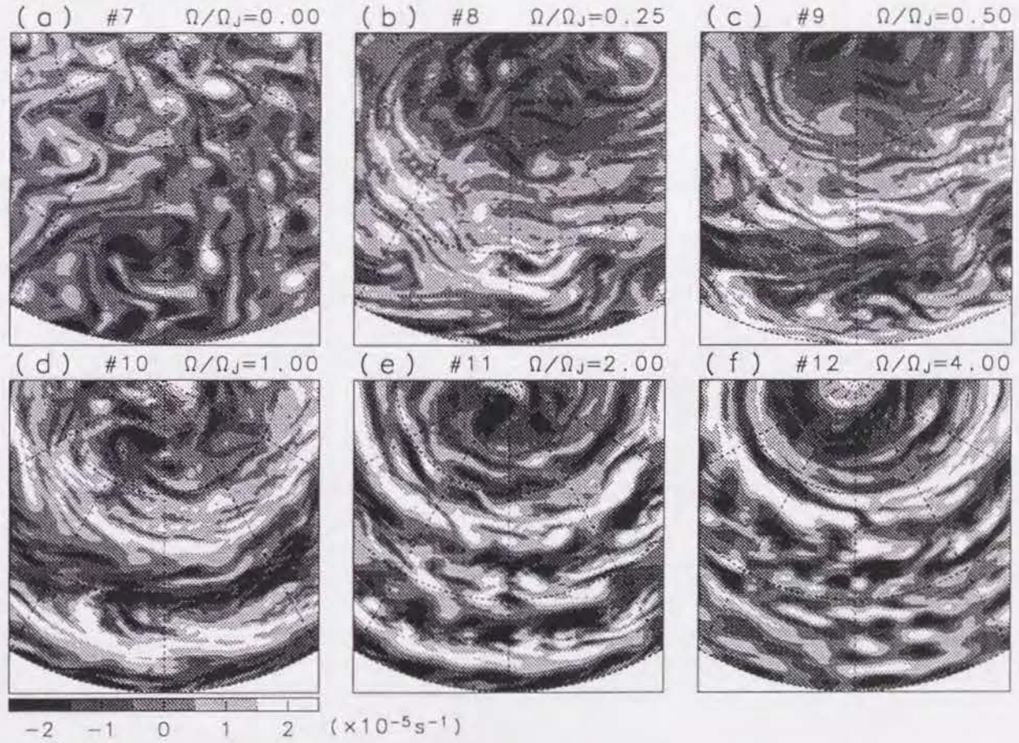

FIG. 5. Relative vorticity field at t = 1000 J.days for the same runs as in Fig.4. Lambert equal area projection from the north pole is used and only a part of the northern hemisphere is shown. Meridians and parallels are shown for every 30°. The central meridian is identical to that in Fig.4.

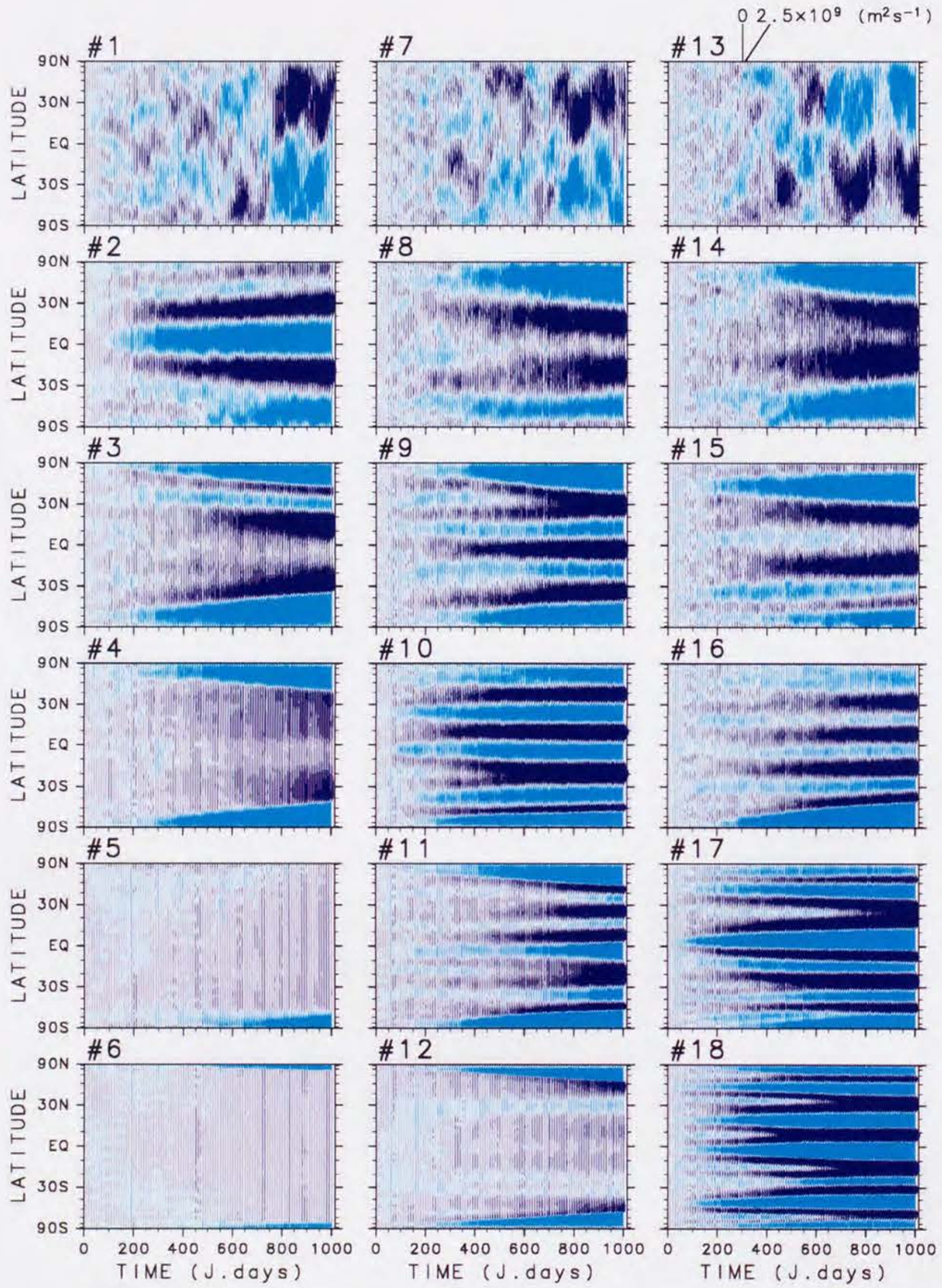

FIG. 6. Temporal variation of the zonal mean zonal angular momentum. Time interval is 10 J.days, and the unit of an interval is 2.5×10^9 m^2 s^{-1}. Westerly zones are in dark blue while easterly zones in light. The number in the upper left of each figure represents the run number. The figures are arranged from top to bottom in the order of the rotation rate Ω/Ω_J, and from left to right in the order of the forcing wavenumber n_f.

3.3 Formation of a zonal band structure

Temporal variation of the zonal mean zonal angular momentum $[\ M\ ] \equiv [\ u\ ]\ a\sqrt{1-\mu^2}$ is shown in Fig.6 for all runs, where $u(\lambda, \mu, t) \equiv -\dfrac{\sqrt{1-\mu^2}}{a}\dfrac{\partial \psi}{\partial \mu}$ is a zonal velocity, and $[\cdots]$ denotes the zonal mean. In the cases of no rotation (#1, #7, #13 ; group **A**), the easterly (light blue) or westerly (dark blue) flow grows in width as the time goes by, and it dominates over a hemisphere by t = 600 J.days or so. The easterly or westerly bands largely vary their positions with time, corresponding to the irregular movement of the large pattern of ψ as seen in Fig.4 (a). For the cases with rotation, on the other hand, the alternating easterly and westerly zonal bands are already discernible in early stages by t = 100 J.days or so, and do not change their positions largely after the establishment of the band structure. They become clear and robust as the rotation rate increases. These zonal band structures can be classified into two groups: one is the alternating easterly and westerly zonal band structure in all the latitudes (#2-3, #8-11, #14-18 ; group **B**), and the other is the circumpolar easterly jets in high latitudes and weak zonal flow in middle and low latitudes for the experiments with a small forcing wavenumber and a large rotation rate (#4-6, #12 ; group **C**). For the group **B**, the number of the bands increases and their width decreases as the rotation rate increases. For large Ω (#9-11, #17-18), several mergers of westerly bands take place and the width of the bands increases during such events. As the time goes by, there is a tendency that the width of easterly bands becomes broad while that of westerly becomes narrow. For the group **C**, on the other hand, position of the circumpolar easterly jets shifts to higher latitudes with an increase in the rotation rate. The width of the easterly flow becomes broad with time as in the group **B**.

Figure 7 shows the time-averaged zonal mean zonal angular momentum $\overline{[\ M\ ]}$ (broken line),

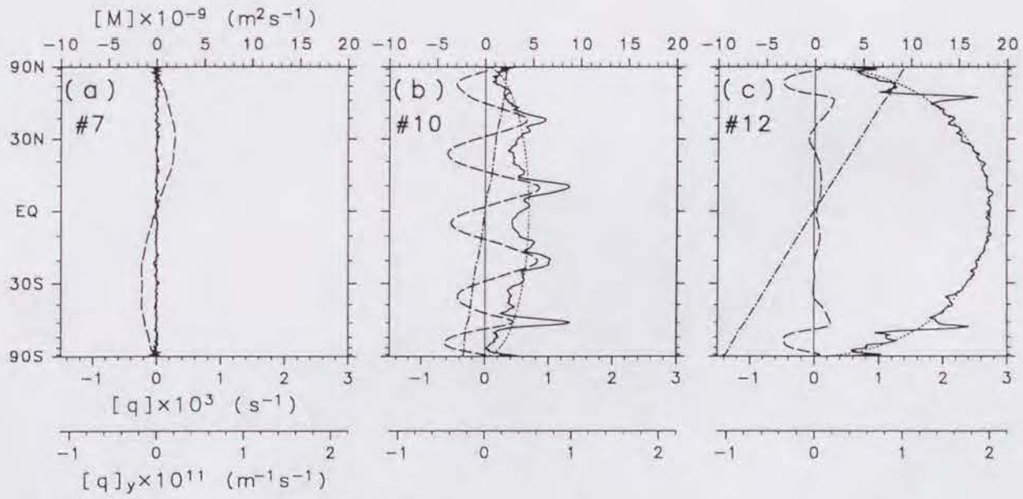

FIG. 7. Meridional distributions of zonal mean zonal angular momentum (broken line), zonal mean potential vorticity (dot-dashed line), meridional gradient of zonal mean potential vorticity (solid line), and that of the planetary vorticity (thin dotted line) for typical three runs of (a) #7, (b) #10, and (c) #12 in series II. Averaged time is from 800 to 1000 J.days.

zonal mean potential vorticity $\overline{[\,q\,]} \equiv \overline{[\,\zeta\,]} + 2\Omega\mu$ (dot-dashed line), and meridional gradient of zonal mean potential vorticity $\overline{[\,q\,]}_y \equiv \dfrac{\sqrt{1-\mu^2}}{a}\dfrac{\partial \overline{[\,q\,]}}{\partial \mu}$ (solid line) for typical three runs of #7(group **A**), #10 (group **B**), and #12(group **C**) in series II. In group **A** without rotation (a), the intensity of $\overline{[\,M\,]}$ is not very large and the region of the easterly or westerly flow extends over a hemisphere as seen in Fig.6. The zonal mean potential vorticity and its meridional gradient is very small in all the latitudes. Although the alternating easterly and westerly jets emerge in all the latitudes in group **B** (b), the zonal mean potential vorticity $\overline{[\,q\,]}$ increases with μ monotonously because of the dominance of the planetary vorticity $2\Omega\mu$. The meridional gradient of the potential vorticity $\overline{[\,q\,]}_y$ is, therefore, positive in all the latitudes indicating that the jets are barotropically stable. The meridional gradient of $\overline{[\,q\,]}$ largely deviates from that of the planetary vorticity $\dfrac{2\Omega}{a}\sqrt{1-\mu^2}$ (thin dotted line), and this deviation is equivalent to a curvature of $\overline{[\,M\,]}$. Thus the westerly jet is narrow and steep while the easterly is broad and gentle. In group **C** in which the circumpolar easterly jets are dominant (c), the meridional gradient of $\overline{[\,q\,]}_y$ is nearly equal to that of the planetary vorticity in the middle and low latitudes (outside of the circumpolar easterly jets) while it becomes nearly constant in high latitudes ; a large gap of $\overline{[\,q\,]}_y$ exists around $\varphi \sim \pm 55°$.

The dependence of the number of jets on the rotation rate is shown in Fig.8. As seen in Fig.6, the number of jets increases with Ω except for the runs in group **C**, in which the zonal mean flow is weak in middle and low latitudes. For the experiments with the same rotation rate, the number of jets is nearly independent of the forcing wavenumber n_f as far as the alternating easterly and westerly jets emerge in the flow field.

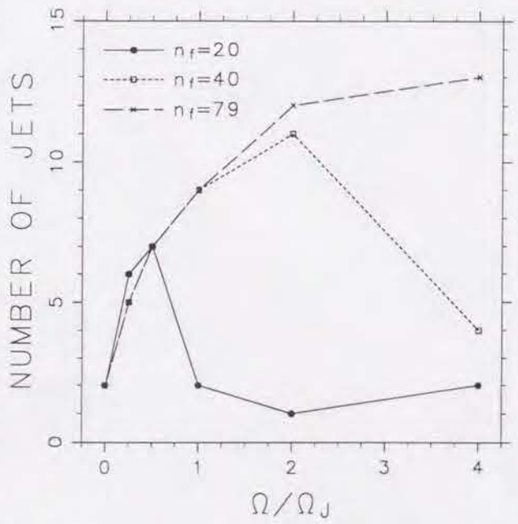

FIG. 8. Dependence of the number of jets on Ω/Ω_J for the runs of series I (solid circles connected by solid line), for those of series II (squares connected by dotted line), and for those of series III (×s connected by broken line).

3.4 Zonal-mean and disturbance fields

In the previous subsections of 3.2 and 3.3, the zonal band structure is dominant in the flow field for the experiments with rotation. Division of the energy spectrum and the flow field into the zonal-mean and disturbance components is, thus, useful to investigate the formation of zonal band structure in detail. Time-wavenumber sections of the energy spectrum for the disturbance $E_{\rm D}(n,t)$ and the zonal-mean components $E_{\rm Z}(n,t)$ are shown Fig.9 for the same three runs as in Fig.7, where the two energy densities are defined as follows :

$$E_{\rm Z}(n,t) = \frac{1}{2}\frac{n(n+1)}{a^2}\mid \psi_n^0(t)\mid^2 , \tag{9}$$

$$E_{\rm D}(n,t) = \frac{1}{2}\sum_{\substack{m=-n \\ m\neq 0}}^{n}\frac{n(n+1)}{a^2}\mid \psi_n^m(t)\mid^2 . \tag{10}$$

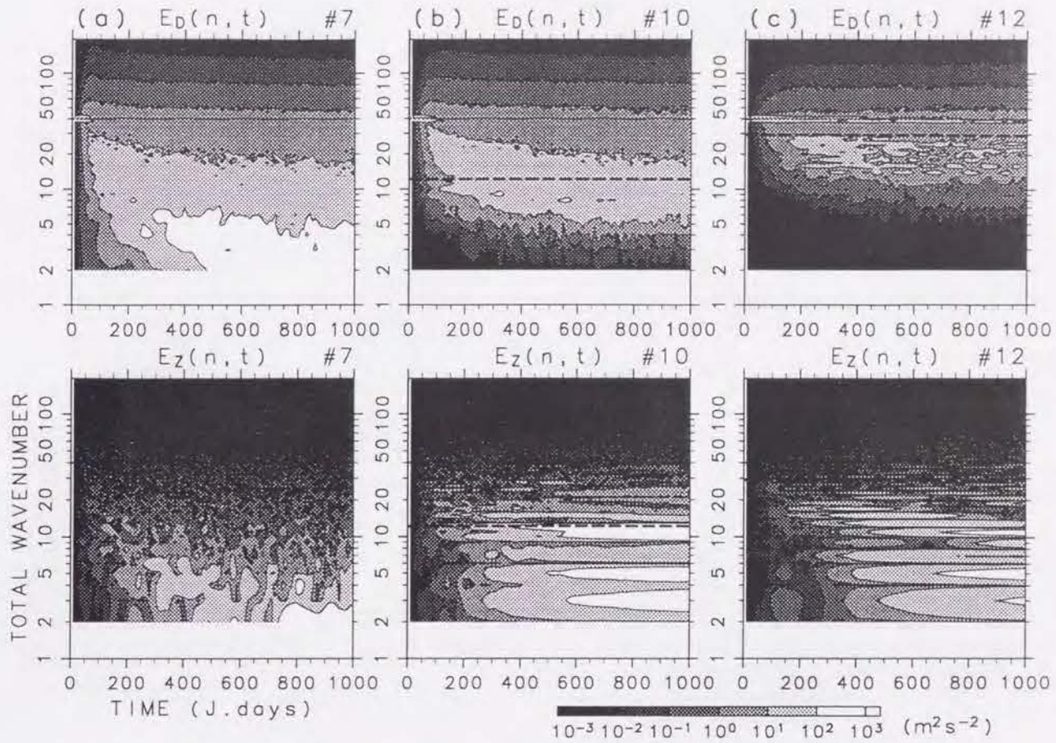

FIG. 9. Time-wavenumber section of energy spectra for the same three runs as in Fig.7. Upper figures show the energy spectrum for disturbances and lower ones for the zonal-mean components. Dotted lines indicate the forcing wavenumber (n_f = 40) and broken lines the wavenumber n_β.

In the case of no rotation (a), the disturbance energy cascades towards the lower wavenumbers as the time goes by, and the spectrum has a maximum at the lowest wavenumber n = 2 by t = 600 J.days or so. The zonal energy also cascades upward and the spectrum has a peak at n = 2 after that time, consistent with the time evolution of [M] (see Fig.6). For the experiment with the rotation Ω_J in group **B** (b), on the other hand, the energy spectrum for the disturbance components has a maximum around $n \sim 10$ after $t \sim 200$ J.days or so, and the distribution of it does not change largely. The upward cascade of the disturbance energy ceases around the wavenumber n_β. The distribution of $E_{\rm Z}(n,t)$ is largely different from that without rotation: the spectral components of the zonal energy, particularly in the low wavenumber range of $2 \leq n \lesssim n_\beta$, begin to increase when the disturbance energy begin to accumulate around the wavenumber n_β. The zonal energy increases with time at several fixed components of the spectrum consistent with the robustness and the persistence of the meridional distribution of [M] as seen in Fig.6. For the run #12 with large Ω of group **C** (c), the time evolution of $E_{\rm D}(n,t)$ and $E_{\rm Z}(n,t)$ is rather similar to those in #10 (b). However, the energy upward cascade for the disturbance components is hard to occur because the wavenumber n_β is very close to the forcing wavenumber n_f. Hence, $E_{\rm D}(n,t)$ has a maximum around the wavenumber n_f for the

whole integration period. The disturbance energy penetrates into the low wavenumber range of $15 \lesssim n \lesssim n_\beta$ and the intensity of it varies with time in this range. The number of spectral components at which the zonal energy is dominant is larger than that in #10.

Figure 10 shows the relative vorticity field for the disturbance components ζ^* and the zonal mean zonal angular momentum [M] at t = 1000 J.days for the same runs as in Figs.7 and 9, where $(\cdots)^* \equiv (\cdots) - [\cdots]$ denotes the disturbance field. In the case of no rotation (a), the disturbance vorticity field is homogeneous and isotropic. The vortex filaments are elongated in various directions insensitive to the distribution of [M]. For the experiment with the rotation Ω_J in group **B** (b), on the other hand, the disturbance vortices are elongated by the shear in the mean zonal flow in the whole sphere. This vortex elongation with systematic alignment brings the intensification of the alternating easterly and westerly zonal jets, suggesting the energy conversion from the disturbance to the zonal-mean components. For the experiment with large Ω of group **C** (c), the disturbance vortices have nearly circular shape in middle and low latitudes, where the shear of [M] as well as the intensity of it is not very large. Thus the zonal mean zonal flow is not intensified. In high latitudes, on the other hand, the vortices elongated by the strong shear of [M], and the circumpolar jet (, or the polar vortex) is intensified.

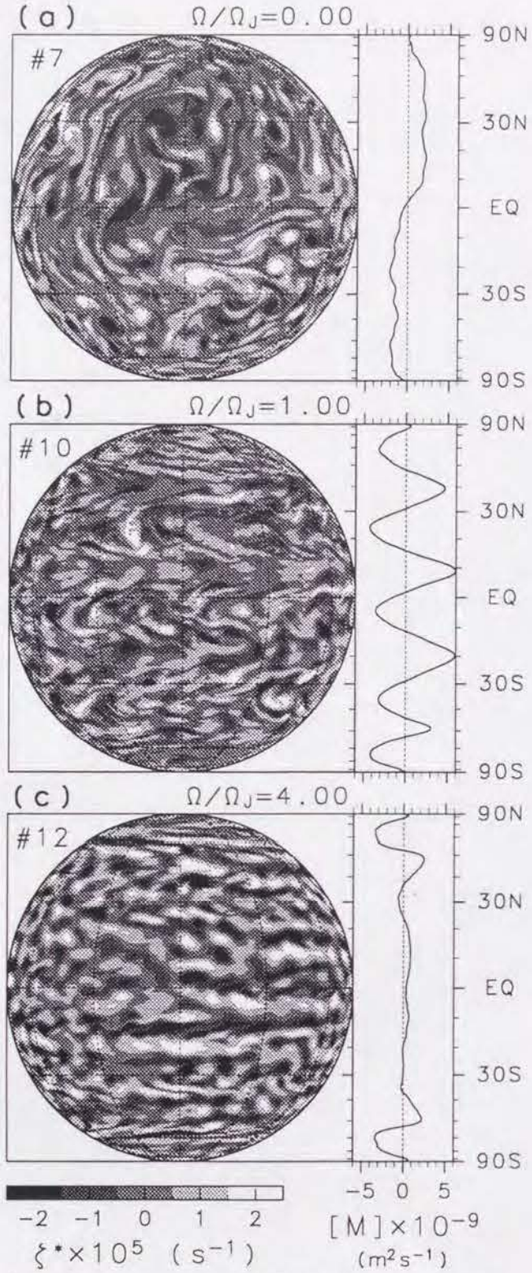

FIG. 10. Relative vorticity field for the disturbance components (left) and zonal mean zonal angular momentum (right) at t = 1000 J.days for the same three runs as in Figs.7 and 9. Map projection is the same as in Fig.1.

3.5 Two-dimensional energy spectrum on a sphere

Figure 11 shows the 2D energy spectral density $E(m, n)$:

$$E(m,n) = \frac{1}{2}\frac{n(n+1)}{a^2}\overline{|\,\psi_n^m(t)\,|^2}\,, \tag{11}$$

in the range of $n \leq 50$ for the same three runs as in Figs.7, 9, and 10. The energy density has the symmetry of $E(-m, n) = E(m, n)$ due to $\psi \in \boldsymbol{R}$, so that it is shown only for $m \geq 0$. In the case of no rotation (a), the energy density increases by the upward energy cascade as the total wavenumber n decreases. The isopleths of $E(m, n)$ is nearly independent of the zonal wavenumber m indicating that the flow field is homogeneous and isotropic as theoretically pointed out by Boer[19]. For the experiments with rotation (b,c), on the other hand, large amount of the energy is found around $m = 0$ at the low wavenumbers of $n \lesssim n_\beta$ and the energy density $E(m, n)$ decreases with an increase in m for fixed n. There is little energy in a segment-shaped region near the lower edge of the triangle, and this region becomes wide as the rotation rate increases (c). Here, the "wave-turbulence boundary" is introduced in the analogy of that in VM for the β-plane turbulence :

$$m = \frac{U}{2\Omega a}n^2(n+1)\,. \tag{12}$$

On this curve, the Rossby wave frequency $\dfrac{2\Omega m}{n(n+1)}$ is equal to the reciprocal of the vorticity advection time Un/a. The curve expressed by Eq.(12) is also drawn in Fig.11 (b,c). The boundary of the segment-shaped region has qualitatively similar shape to this curve, although these two curves quantitatively disagree. Even in the range of $n \gtrsim n_\beta$, the isopleths of $E(m, n)$ is not horizontal in this diagram but it has a gradual gradient with m.

Figure 12 also shows $E(m, n)$ in the full wavenumber range for other three runs of #1, #3, and #6 in series I with the forcing of small wavenumbers. In contrast to the runs in Fig.11, these

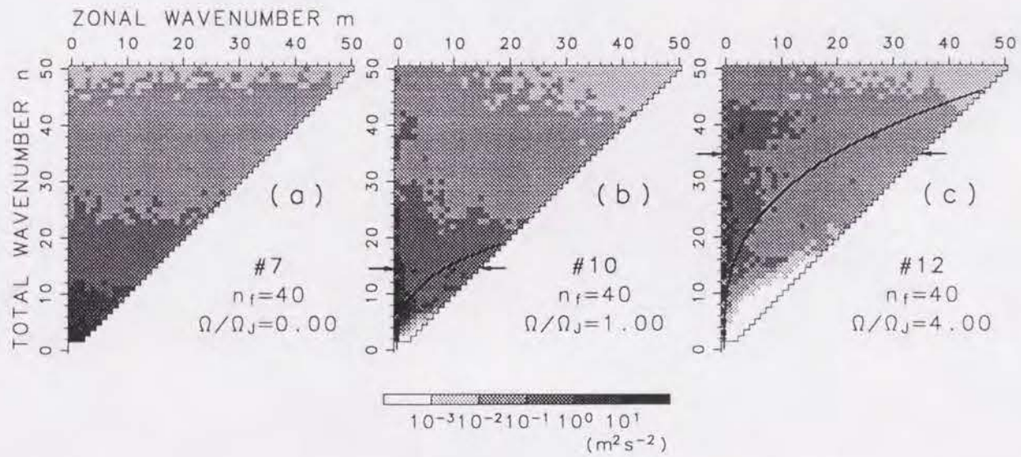

FIG. 11. Two-dimensional energy density averaged from 800 to 1000 J.days for the same three runs as in Figs.7, 9, and 10. Low-wavenumber region of $0 \leq m, n \leq 50$ is shown. Thick arrows represent the wavenumber n_β. Solid curves indicate the "wave-turbulence boundary" at which the inverse of the vorticity advection time is comparable to the Rossby wave frequency.

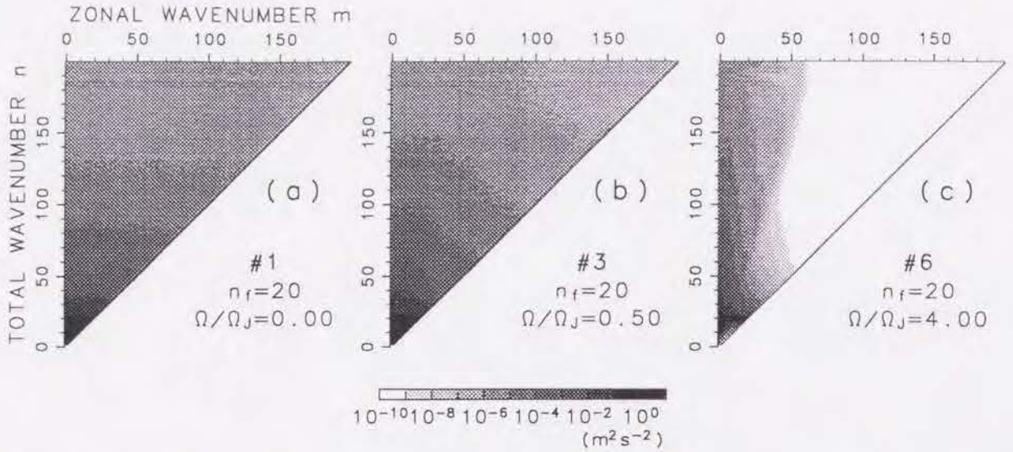

FIG. 12. Two-dimensional energy density averaged from 800 to 1000 J.days for typical three runs of (a) #1, (b) #3, and (c) #6 in series I. Full components are shown.

are chosen here to clarify the spectral anisotropy in the high-wavenumber region far away from the forcing. In the case of no rotation (a), the isopleths of $E(m,n)$ is nearly independent of m, so that the flow field is homogeneous and isotropic in all the wavenumber range. For the experiments with rotation, on the other hand, the isopleths has a gradient with m even in the high-wavenumber region. When the rotation rate is large (c), the isopleths of $E(m,n)$ is nearly vertical in this diagram and most of the energy is confined in the wavenumber region of $m \lesssim 50$ indicating a strong zonal anisotropy for all the range of n.

3.6 Two-dimensional energy spectrum on a tangential plane

In this subsection, we compare local feature of the 2D turbulence on the spherical geometry with some numerical results obtained on a β-plane[13] by introducing a square tangential plane whose center is (λ_c, φ_c) and side is equal to the radius of the sphere a. The flow field on the sphere is orthographically projected on the plane. Twenty-five tangential planes are selected to cover all around the sphere considering the ratio of areas : nine planes in the equatorial region ($\varphi_c = 0°$) with equal longitudinal difference of $\Delta\lambda_c = 40°$, twelve in the middle latitudes ($\varphi_c = \pm 45°$) with $\Delta\lambda_c = 60°$, and four in the polar region ($\varphi_c = \pm 90°$) with two different orientations (45°) for each pole. The streamfunction field $\psi(x,y,t)$ on an equatorial tangential plane at $t = 1000$ J.days is shown in Fig.13 (a) for the run #7, where x and y are the abscissa and ordinate of the plane, respectively. If the energy density is calculated from this streamfunction field, discontinuity of $\psi(x,y,t)$ at the boundaries brings an aliasing error to the spectrum. To reduce the effect of the discontinuity, a modified streamfunction $\Psi(x,y,t)$ is defined as follows :

$$\Psi(x,y,t) = \frac{\psi(x,y,t) - \psi_r(x,y,t)}{\sqrt{\langle\langle\{\psi(x,y,t) - \psi_r(x,y,t)\}^2\rangle\rangle}}, \tag{13}$$

where $\psi_r(x,y,t)$ is a regression plane obtained from the streamfunction $\psi(x,y,t)$ by the least squared method, and $\langle\langle\cdots\rangle\rangle$ indicates the area average on the tangential plane. The modified streamfunction field $\Psi(x,y,t)$ exhibits a normalized deviation of $\psi(x,y,t)$ from the regression

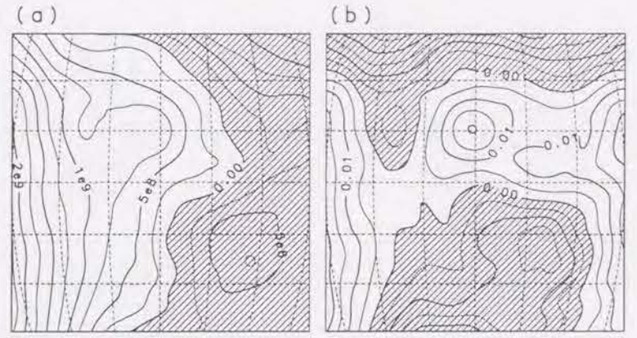

FIG. 13. **(a) :** Streamfunction field $\psi(x,y)$ at $t = 1000$ J.days for the run #7. The streamfunction is orthographically projected on an equatorial tangential plane. Meridians and parallels are drawn for every 10°. Contour interval is 2.5×10^8 $m^2 s^{-1}$ and negative areas are shaded. **(b) :** Modified streamfunction field $\Psi(x,y)$; deviation of the streamfunction $\psi(x,y)$ from a regression plane $\psi_r(x,y)$, which is calculated from ψ by the least squared method. The amplitude of Ψ is normalized as the area average of Ψ^2 becomes unity (see text for definition). Contour interval is 5×10^{-3} and negative areas are shaded.

plane $\psi_r(x,y,t)$. In addition, the sides of the tangential plane are normalized to 2π. Figure13 (b) shows the modified streamfunction field $\Psi(x,y,t)$ obtained from $\psi(x,y,t)$ in Fig.13 (a).

The 2D energy spectral density $E(k,l)$ is calculated from the modified streamfunction field $\Psi(x,y,t)$ as follows :

$$E(k,l) = \frac{k^2+l^2}{2} \mid \Psi_l^k(t) \mid^2, \tag{14}$$

where k and l are x- and y-wavenumbers, respectively, and $\Psi_l^k(t)$ is an expansion coefficient of Fourier transformation of $\Psi(x,y,t)$:

$$\Psi_l^k(t) = \int_0^{2\pi}\int_0^{2\pi} \Psi(x,y,t) e^{-i(kx+ly)} dx dy . \tag{15}$$

The numbers of grid points are 96^2 on the tangential plane, so that the truncation wavenumber is 48. For this resolution, the forcing wavenumbers $n_f = 20$, 40, and 79 on the sphere roughly correspond to the wavenumbers $\kappa_f = \sqrt{k_f^2 + l_f^2} = 3$, 6, and 12, respectively. Figure 14 shows the time-averaged 2D energy density $\overline{E(k,l)}$ for the same run as in Fig.13 without rotation (group **A**). Twenty-five energy densities for each plane are also averaged. The energy density $\overline{E(k,l)}$ roughly shows a homogeneous and isotropic distribution, although the effect of the aliasing error remains around the lines $k = 0$ and $l = 0$.

The modified streamfunction fields $\Psi(x,y,t)$ at $t = 1000$ J.days are shown in Fig.15 (a-c) for the run #10 with moderate rotation rate ($\Omega/\Omega_J = 1.00$; group **B**). On equatorial- and mid-latitude tangential planes (a,b) the zonal band structure is dominant, although the bands have

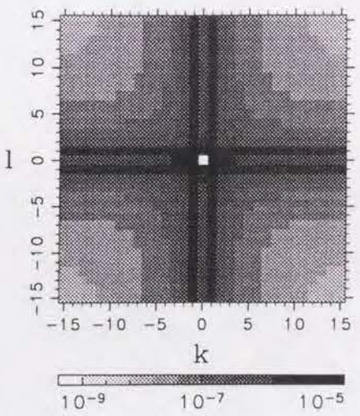

FIG. 14. Two-dimensional energy density calculated from the modified streamfunction field for the same run as in Fig.13. Time averages from 800 to 1000 J.days and ensemble averages of 25 cases of the tangential planes.

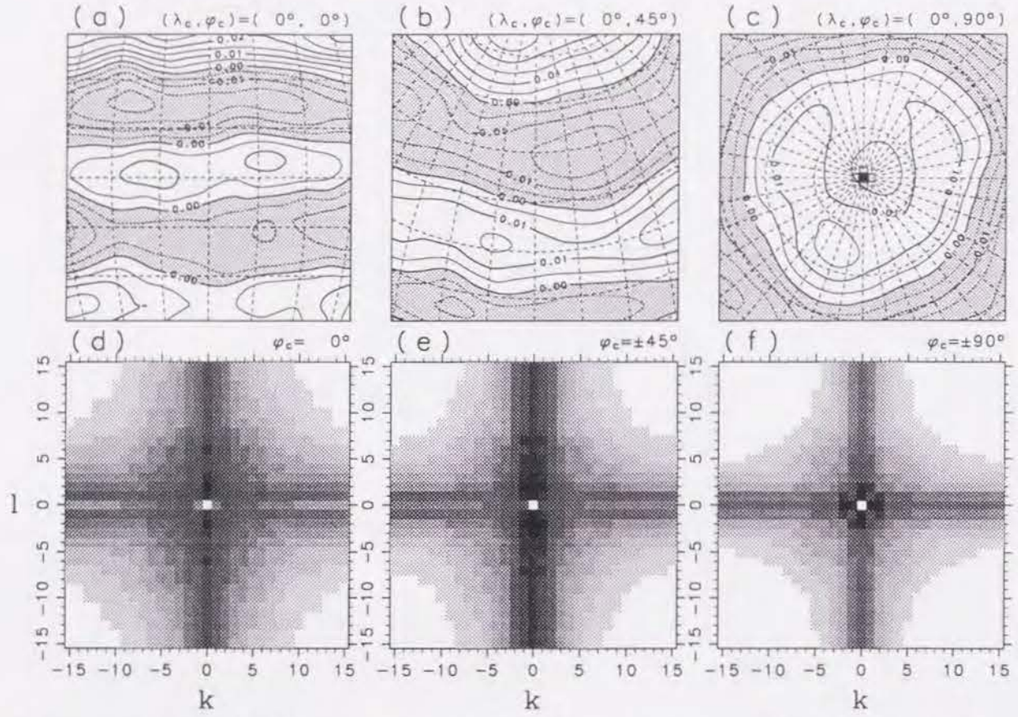

FIG. 15. **(a-c) :** Modified streamfunction field $\Psi(x, y)$ at t = 1000 J.days for the run #10. The center of the tangential plane (λ_c, φ_c) is indicated on the top of each figure. **(d-f) :** Two-dimensional energy density calculated from the modified streamfunction field for the run #10. The number in the upper right of each figure represents the central latitude φ_c of the tangential plane. Time averages from 800 to 1000 J.days and ensemble averages of (d) 9 cases, (e) 12 cases, and (f) 4 cases. Shading is done by the same color code as in Fig.14.

a little curvature in middle latitudes (b). On the other hand, a coaxial circular structure dominates on a polar tangential plane (c). Figure 15 (d-f) shows the 2D energy density $\overline{E(k,l)}$ for this run. In the tangential planes in low and middle latitudes (d,e), the energy distribution is rather anisotropic owing to the β-effect ; the energy around $k = 0$ is large and the isopleths of $\overline{E(k,l)}$ is elongated in the direction of l-axis. The energy density is large on the horizontal lines of $l = \pm 1$ nearly independently of the wavenumber k. The difference of the spectral anisotropy is not significant between equatorial region (d) and middle latitudes (e). In the polar tangential planes (f), on the other hand, the distribution of the energy is clearly isotropic except for the aliasing. This isotropic distribution of $\overline{E(k,l)}$ is rather different from that for #7 without rotation (Fig.14) ; the energy is confined into smaller wavenumber region.

The the modified streamfunction field (a-c) and energy density $\overline{E(k,l)}$ (d-f) for the run #12 with large rotation rate ($\Omega/\Omega_J = 4.00$; group **C**) are shown in Fig.16. The spectral anisotropy is evident in the equatorial region (d) and the energy density $\overline{E(k,l)}$ shows clear dumbbell shape at the low wavenumber region. The dumbbell shape reminds us of the original finding by VM in their β-plane experiment. The energy has a maximum at relatively large meridional wavenumbers around $l = \pm 5$ corresponding to the zonal band structure in the streamfunction field (a). Similar spectral anisotropy is obtained in middle latitudes (e) except for the dumbbell shape.

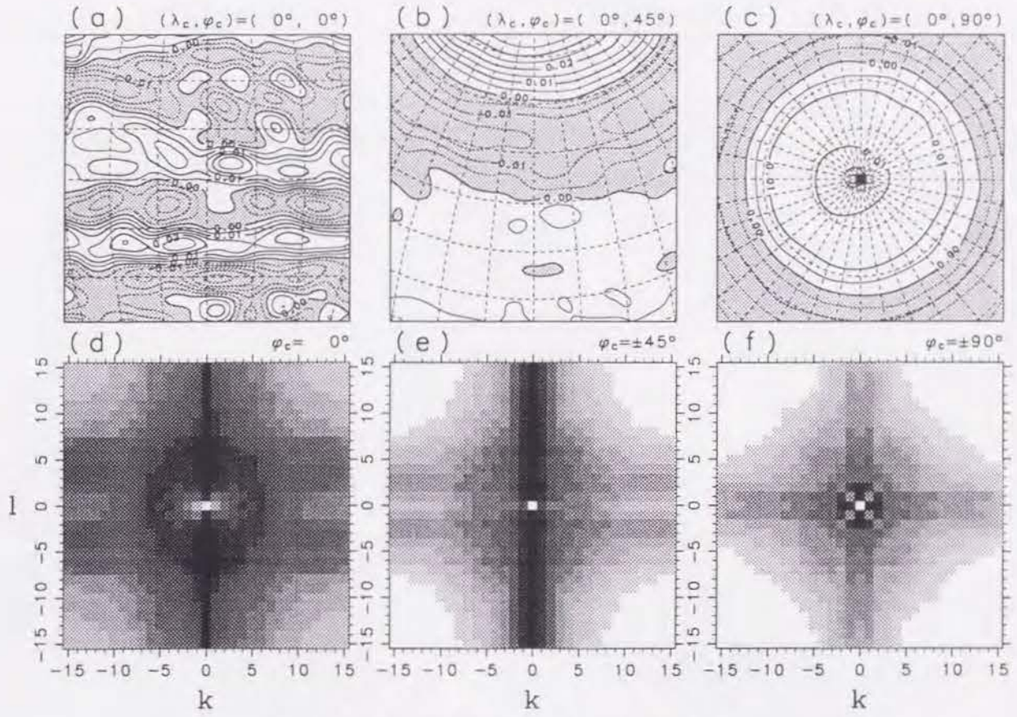

FIG. 16. As in Fig.15 but for the run #12.

4 DISCUSSIONS

For the 2D turbulence with the effect of differential rotation, Maltrud & Vallis[12] have already studied the energy transfer in their numerical experiments on a β-plane. They showed that the transferred energy accumulates near k_β owing to the suppression of the upward energy cascade by the rotation, and that the power law in the energy-cascading range remains nearly proportional to $k^{-5/3}$. Although the wavenumber n_β we used is not identical to k_β, these features of the energy spectrum influenced by the rotation are obtained in our experiments with small and moderate rotation rates (Fig.2). For the cases with larger rotation rate ($\Omega/\Omega_J \geq 2.00$), the process of the energy interchange is largely influenced by the rotation and the energy is accumulating even in the energy-cascading range. Hence the energy spectrum in this range becomes steeper than $n^{-5/3}$ as shown in Fig.2 (#11, #17 and #18). When the forcing wavenumber is small and the rotation rate is large, on the other hand, the wavenumber n_β is nearly equal to or larger than the forcing wavenumber n_f, and the upward energy cascade is largely suppressed by the effect of rotation as shown in Fig.3 (#4-6, and #12). The enstrophy cascade is also suppressed, because the normal enstrophy cascade is strongly connected with the upward energy cascade. Thus the energy spectrum is steeper than n^{-4} in the enstrophy-cascading range for these experiments.

Some clear band structures are emerged in the flow field in this study using the full spherical model and the isotropic vorticity forcing function. Nearly two decades ago Williams[15] studied the forced 2D turbulence with a longitudinally cyclic boundary condition and an anisotropic forcing function, and he showed an impressive clear band structure. However, the zonality of the flow field he obtained is much stronger than that obtained in this study for similar experi-

mental parameters as shown in Fig.4 (d); thus his result is more or less influenced by the cyclic boundary condition and by the anisotropic forcing function. Basdevant *et al.*[10] did a few numerical experiments on the forced 2D turbulence on a full sphere, but such a clear zonal band structure as shown in Fig.4 (d,e) did not emerge because of the smallness of the rotation rate and of the introduction of low-wavenumber dissipation in their experiments.

Yoden & Yamada[16] showed the emergence of strong circumpolar vortices with easterly jets in the numerical experiments on decaying 2D turbulence on a rotating sphere starting from many initial flow fields with the energy spectrum that has a maximum at a low wavenumber $n = 10$. Similar flow pattern is obtained in this study for the experiment with the forcing wavenumber $n_f = 40$ and a large rotation rate $\Omega/\Omega_J = 4.00$ as shown in Fig.4 (f), and it emerges even for the cases with smaller rotation rate for the smaller forcing wavenumber $n_f = 20$ (#4-6 in Fig.6). Thus the emergence of the strong circumpolar vortices with easterly jets in their experiments might be due to the smallness of the wavenumber where the energy spectrum has a maximum initially. On the other hand, the most poleward jet (i.e., circumpolar jet) obtained here is easterly for all the runs as seen in Fig.6. Hence the emergence of easterly circumpolar jets in high latitudes seems to be a general feature of both decaying and forced 2D turbulence on a rotating sphere.

The alternating easterly and westerly zonal band structure was found in the numerical experiments on a 2D β-plane turbulence by Vallis & Maltrud[13] as well as in the experiments on a quasigeostrophic two-layer β-plane turbulence by Panetta[14]. Both experiments showed that the westerly flow is narrower and sharper than the easterly. Similar difference between the westerly and the easterly flow is also seen in this study; the westerly flow becomes narrow and sharp while the easterly becomes wide and gentle as the time goes by (Figs.6 and 7). The zonal band structure with narrow westerly and wide easterly is a common feature for the forced 2D turbulence both on a β-plane and on a rotating sphere. Furthermore, in Fig.6, we can see another difference between the westerly and the easterly flow that several mergers of the westerlies take place but merger of the easterlies does not occur in the time evolution of the zonal flow field. These difference between the easterly and the westerly flows might be produced by meridionally propagating Rossby wave packets, which may redistribute the zonal mean zonal angular momentum to maintain the band structure resulting in such a remarkable difference.

In the present study, the zonal band structure is formed in early stages and then it becomes robust and persistent for the cases with rotation in group **B** as shown in Fig.6. After the establishment of the band structure ($t \gtrsim 200$ J.days), the disturbance energy is transferred into the zonal mean flow owing to the distortion of the disturbance vortices by the shear in the zonal mean flow as studied by Shepherd[11] in the numerical experiments on 2D turbulence on a β-plane under the existence of an imposed large-scale zonal jet. This straining of the disturbance vortices by the shear seems to be a fundamental dynamics of the formation and maintenance of the band structure for the cases in group **B** as shown in Figs.9 and 10.

For the runs with small rotation rates, the flow field has an alternating easterly and westerly zonal band structure and number of zonal jets as well as width of them is nearly independent of the forcing wavenumber if the value of the rotation rate is identical (e.g. #2, #8, and #14 in Fig.6). On the other hand, the emerged structure is very sensitive to the forcing wavenumber when the rotation rate is large: the alternating zonal bands emerge for the runs with large forcing wavenumber in group **B** while strong circumpolar easterly jets and weak westerly flow in middle

and low latitudes emerge for the runs with small forcing wavenumber in group **C**. In group **B**, vortex straining by the shear in the mean zonal flow is dominant in the whole sphere as in the cases with small rotation rate. In group **C**, however, simple Rossby-wave propagation without strong interactions with the mean zonal flow is dominant in middle and low latitudes as seen in Fig.5 (f) and Fig.10 (c). This difference in the flow field between group **B** and group **C** suggests the importance of the effect of rotation even in such a small scale of the vorticity forcing.

The 2D energy density diagnosed on the spherical domain shows anisotropic distribution for the experiments with rotation ; there is little energy in a characteristic segment-shaped region near the lower edge of the triangular wavenumber space (Fig.11 (b,c)). The spherical version of the "wave-turbulence boundary" introduced by Vallis & Maltrud[13] exhibits qualitatively similar segment shape. However, the boundary largely overpredicts the outline of the energy distribution as seen in Fig.11 (c) in contrast with the case on a β-plane. Thus some modification of the "wave-turbulence boundary" is necessary for the spherical geometry.

Boer & Shepherd[20] analyzed the global FGGE dataset to investigate several aspects of large-scale turbulence in the atmosphere on the basis of the homogeneous and isotropic 2D turbulence on a sphere. Vertically integrated kinetic energy spectrum in their results shows a similar segment-shaped region in which little energy exists at the low-wavenumber region of $m, n \lesssim 5$ as seen in the present study (Fig.11 (b,c)). This correspondence suggest the two-dimensional Rossby-wave / turbulence nature of the large-scale atmospheric motion.

The spectral anisotropy is also found in high wavenumber region of the triangular wavenumber space as well as in low wavenumber region (Fig.12 (b,c)) ; the energy density decreases as the zonal wavenumber m increases. This tendency of the zonal anisotropy in high wavenumbers was already obtained by Holloway & Hendershott[9] and Basdevant *et al.*[10] in their experiments on the 2D turbulence on β-planes. Thus the spectral anisotropy in zonal direction is a common feature of the 2D turbulence on a rotating sphere and on a β-plane. It is necessary to investigate the reason why the energy density distributes anisotropically even in the high-wavenumber region where the effect of rotation is very small.

As seen in Fig.14, the 2D energy density calculated from the local flow field projected on a tangential plane shows the isotropy of the energy distribution in the case without rotation, because the flow field is homogeneous and isotropic. The isotropic distribution of the 2D energy density is also obtained for the runs with rotation in the polar tangential plane (Fig.15 (f) and Fig.16 (f)). In this case, however, a circumpolar vortex is dominant in the flow field, so that the flow field is isotropic with respect to the center of the vortex as seen in Fig.15 (c) and Fig.16 (c).

When the flow field is projected on an equatorial tangential plane, the 2D energy density shows clear dumbbell shape in low wavenumber region as in VM for the runs with large rotation rate (Fig.16 (d)). The wavenumber k_β estimated for the equatorial tangential plane with the value of β at the equator (the second last column in Table I) is somewhat larger than the wavenumber of the boundary on the k-axis, and this tendency of overprediction is also obtained by VM. For the flow fields projected on mid-latitude tangential planes, on the other hand, the 2D energy density does not show such clear dumbbell shape even in the runs with large rotation rates (Fig.16 (e)). In these cases, the modified streamfunction field has a little curvature, particularly in higher latitudes as seen in Fig.16 (b). Furthermore, the β-plane approximation is not so good. Thus the energy density may not exhibit clear dumbbell shape.

5 CONCLUSIONS

In this thesis, the studies were intended to get deep understandings of the nature of the forced two-dimensional turbulence on a rotating sphere by numerical methods. A series of numerical experiments on the forced 2D turbulence on a rotating sphere were done with a high-resolution barotropic model which has the term of homogeneous and isotropic vorticity forcing. The formation of the zonal band structure and the spectral anisotropy were investigated by sweeping two experimental parameters of the rotation rate and the forcing wavenumber.

For the runs without rotation, the energy is transferred to the lowest wavenumber of $n = 2$ and it accumulates around this wavenumber owing to the finiteness of the spherical domain. For the runs with rotation, on the other hand, the upward energy cascade ceases around a characteristic wavenumber n_β at which the "β-term" due to the planetary rotation is comparable to the nonlinear Jacobian term, and the transferred energy accumulates in the range of $n \lesssim n_\beta$. As the rotation rate increases, the energy-cascading range becomes narrow, although the slope in this range remains close to $n^{-5/3}$. When the wavenumber n_β is nearly equal to or larger than the forcing wavenumber n_f, the upward energy cascade is strongly inhibited by the effect of rotation.

In the cases of no rotation (we called group **A**), the streamfunction field shows a very large flow pattern because the energy cascades upward to the lowest wavenumber, so that the easterly or westerly flow dominates over a hemisphere. In the vorticity field, a lot of vorticity patches with circular structure are dominant. For the experiments with rotation (group **B**), on the other hand, a zonal band structure which consists of the alternating easterly and westerly jets becomes dominant in the streamfunction field. Width of the jets decreases and number of them increases as the rotation rate increases. The band structure is already discernible in early stages of the time integration from the initial condition of no flow field, and it is robust and persistent for the integration period of 1000 Jovian days. The easterly jets become broad and gentle while the westerly ones becomes narrow and sharp. In the vorticity field, patches of large vorticity get elongated zonally and the alternating positive and negative vorticity bands emerge. For the experiments with small forcing wavenumber and large rotation rate (group **C**), the zonal band structure is confined in high latitudes with the emergence of the circumpolar vortex with strong easterly jets. The position of the circumpolar easterly jets shifts into high latitudes as the rotation rate increases. Outside of the polar vortex, mean zonal flow is weak westerly in middle and low latitudes, and nearly circular vorticity patches are dominant in the vorticity field.

The process of the formation of a zonal band structure is studied by dividing the vorticity field and the energy spectrum into the zonal-mean and disturbance components. For the runs without rotation, the energy for disturbance components as well as that for the mean zonal flow is transferred to the lowest wavenumber of $n = 2$. For the runs with rotation, on the other hand, the upward cascade of the disturbance energy ceases around the wavenumber n_β. The transferred disturbance energy is converted to several components of zonal energy in the low wavenumber range of $2 \leq n \lesssim n_\beta$. This energy conversion corresponds to the straining of disturbance vortices by the shear in the mean zonal flow, and the elongated vortices with systematic alignment intensify the alternating easterly and the westerly zonal jets.

The 2D energy density in the spherical domain exhibits the isopleths independent of the zonal wavenumber m for the runs without rotation, indicating that the flow field is homogeneous and

isotropic. In the case with rotation, on the other hand, large amount of energy is in the range of $2 \leq n \lesssim n_\beta$ with $m = 0$, while little energy is found in a characteristic segment-shaped region near the lower edge of the triangular wavenumber space. The segment-shaped region becomes wide as the rotation rate increases. The 2D energy density in the high wavenumber region also shows anisotropic distribution as well as in the low wavenumber region ; most of the energy is confined in the lower zonal wavenumbers for all the range of n. The confinement becomes more evident as the rotation rate increases.

For some experiments, the flow field on the spherical geometry was projected orthographically on some tangential planes to compare the energy density distributions in 2D wavenumber space with those obtained in some β-plane experiments. In the case without rotation, the 2D energy density shows the homogeneous and isotropic distribution. For the runs with rotation, on the other hand, the distribution of the 2D energy density largely depends on the value of β at the center of the plane. In the equatorial tangential planes, the 2D energy density shows anisotropic distribution. The isopleths is elongated elliptically in the direction of meridional wavenumber, and the energy is accumulated within small zonal wavenumbers. There are other accumulations along constant meridional wavenumbers due to the emergence of a zonal band structure in the flow field. The 2D distribution in low wavenumbers shows the characteristic dumbbell shape of little energy density as shown in Vallis & Maltrud[13]. Similar anisotropic features are obtained in the mid-latitude tangential plane except for the dumbbell shape in the low wavenumber region. In the polar tangential plane the distribution of 2D energy density is isotropic, because the circumpolar vortex dominates over the plane.

All of the studies in this thesis were made through intensive discussions with the author's supervisor, Dr. S. Yoden. Hence, it is rather difficult to separate the author's original contribution in each study. However, basic ideas on the division of the energy spectrum and the flow field into the zonal-mean and disturbance components (subsection 3.4) and the analysis of the 2D energy spectral density on the tangential planes (subsection 3.6) were got by himself. All of the computation were done by the author.

ACKNOWLEDGEMENTS

The author would like to thank Dr. S. Yoden for his continuing guidance and valuable discussions throughout this work. Thanks are also due to Professor I. Hirota for his valuable comments and encouragement. The author is also grateful to Drs. M. Shiotani, K. Sato, and K. Ishioka and colleagues in the author's laboratory for their helpful discussions and technical support.

REFERENCES

[1] R. H. Kraichnan, "Inertial ranges in two-dimensional turbulence," Phys. Fluids **10**, 1417 (1967).

[2] C. E. Leith, "Diffusion approximation for two-dimensional turbulence," Phys. Fluids **11**, 671 (1968).

[3] D. K. Lilly, "Numerical simulation of two-dimensional turbulence," Phys. Fluids **12(Suppl. II)**, 240 (1969).

[4] U. Frisch, and P. L. Sulem, "Numerical simulation of the inverse cascade in two-dimensional turbulence," Phys. Fluids **27**, 1921 (1984).

[5] B. Legras, P. Santangelo, and R. Benzi, "High resolution numerical experiments for forced two-dimensional turbulence," Europhys. Lett. **5**, 37 (1988).

[6] J. C. McWilliams, "The emergence of isolated coherent vortices in turbulent flow," J. Fluid Mech. **146**, 21 (1984).

[7] P. Santangelo, R. Benzi, and B. Legras, "The generation of vortices in high resolution, two-dimensional decaying turbulence and the influence of initial conditions on the breaking of self-similarity," Phys. Fluids A **1**, 1027 (1989).

[8] P. B. Rhines, "Waves and turbulence on a beta-plane," J. Fluid Mech. **69**, 417 (1975).

[9] G. Holloway, and M. Hendershott, "Stochastic closure for nonlinear Rossby waves," J. Fluid Mech. **82**, 747 (1977).

[10] C. Basdevant, B. Legras, R. Sadourny, and M. Beland, "A study of barotropic model flows : intermittency, waves and predictability," J. Atmos. Sci. **38**, 2305 (1981).

[11] T. G. Shepherd, "Rossby waves and two-dimensional turbulence in a large-scale zonal jet," J. Fluid Mech. **183**, 467 (1987).

[12] M. E. Maltrud, and G. K. Vallis, "Energy spectra and coherent structures in forced two-dimensional and beta-plane turbulence," J. Fluid Mech. **228**, 321 (1991).

[13] G. K. Vallis, and M. E. Maltrud, "Generation of mean flows and jets on a beta plane and over topography," J. Phys. Oceanogr. **23**, 1346 (1993).

[14] R. L. Panetta, "Zonal jets in wide baroclinically unstable regions: Persistence and scale selection," J. Atmos. Sci. **50**, 2073 (1993).

[15] G. P. Williams, "Planetary circulations: 1. Barotropic representation of Jovian and terrestrial turbulence," J. Atmos. Sci. **35**, 1399 (1978).

[16] S. Yoden, and M. Yamada, "A numerical experiment on two-dimensional decaying turbulence on a rotating sphere," J. Atmos. Sci. **50**, 631 (1993).

[17] T. Nozawa, and S. Yoden, "Formation of zonal band structure in forced two-dimensional turbulence on a rotating sphere," *submitted to* Phys. Fluids.

[18] T. Nozawa, and S. Yoden, "Spectral anisotropy in forced two-dimensional turbulence on a rotating sphere," *submitted to* Phys. Fluids.

[19] G. J. Boer, "Homogeneous and isotropic turbulence on the sphere," J. Atmos. Sci. **40**, 154 (1983).

[20] G. J. Boer and T. G. Shepherd, "Large-scale two-dimensional turbulence in the atmosphere," J. Atmos. Sci. **40**, 164 (1983).